Volume 40
Number 3
March 2025
Pages 531–922

JAAS

Journal of Analytical Atomic Spectrometry

rsc.li/jaas

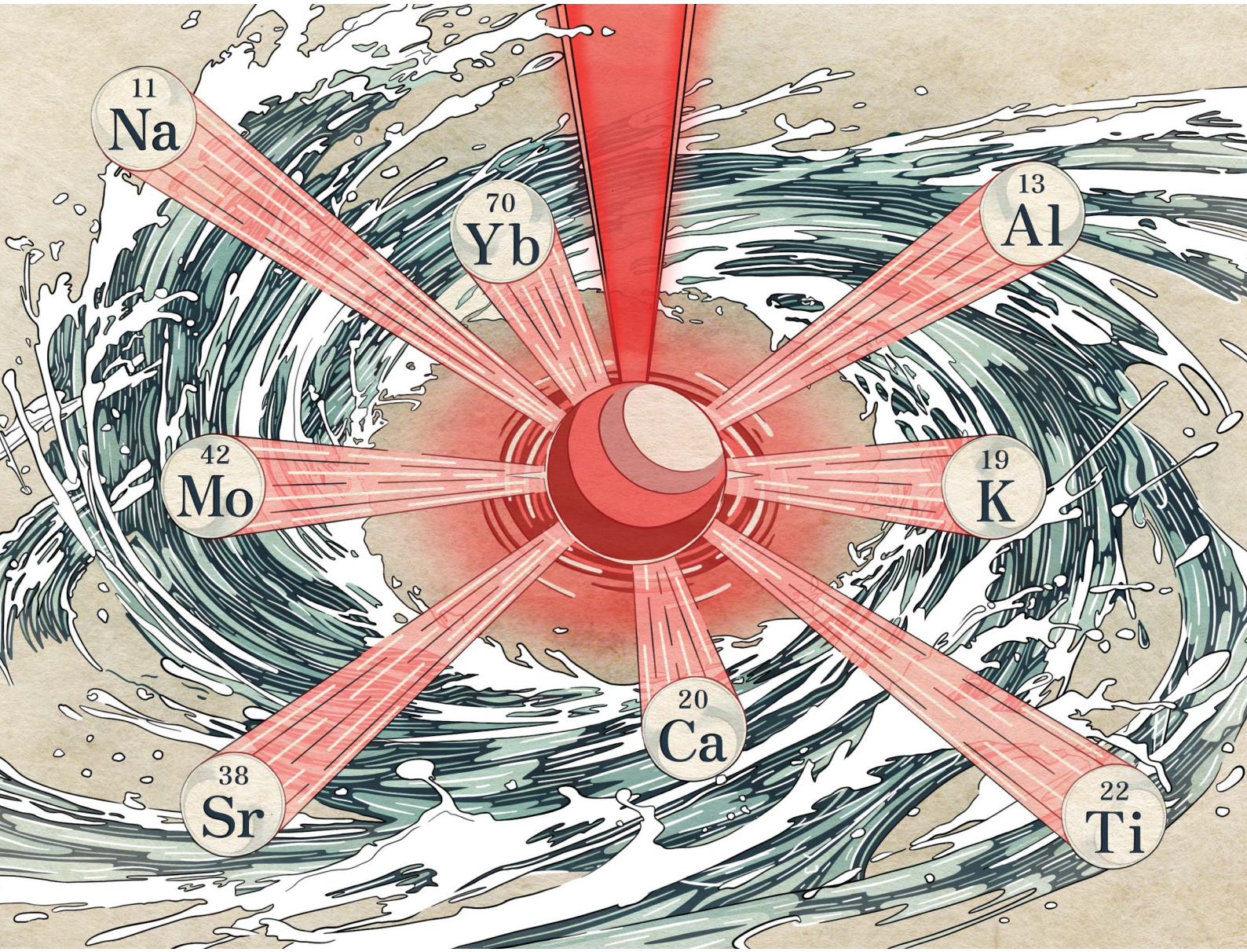

ISSN 0267-9477

ROYAL SOCIETY OF CHEMISTRY

PAPER

H. B. Andrews *et al.*

Real-time elemental analysis of liquids for process monitoring using laser-induced breakdown spectroscopy with a liquid wheel sampling approach

JAAS

PAPER

View Article Online
View Journal | View Issue

Cite this: *J. Anal. At. Spectrom.*, 2025, 40, 689

Real-time elemental analysis of liquids for process monitoring using laser-induced breakdown spectroscopy with a liquid wheel sampling approach†‡

H. B. Andrews, *[a] Z. B. Kitzhaber, [a] B. T. Manard, [b] M. Z. Martin [c] and L. R. Sadergaski [a]

This article presents an engineered sampling system that used a rotating wheel to form a thin liquid layer, permitting the use of laser-induced breakdown spectroscopy (LIBS) for *in situ*, real-time elemental impurity quantification during liquid processing. The sampling approach was demonstrated on eight elements from across the periodic table (Na, Al, K, Ca, Ti, Sr, Mo, and Yb). Univariate and multivariate calibrations were presented for each element. The average value for percent root mean square errors of cross-validation for the multivariate models was 3.64%, highlighting the method's strong prediction accuracy. Additionally, the limits of detection for each analyte were estimated from their univariate models: Na = 0.0532, Al = 18.5, K = 0.105, Ca = 0.273, Ti = 67.7, Sr = 0.640, Mo = 22.4, and Yb = 22.9 μg mL^{-1}. Finally, a test in which multivariate models were used to monitor a liquid system for 80 min was performed to investigate the real-time monitoring capabilities of this liquid LIBS sampling approach. Rigorous measurements were performed to effectively predict the absence and concentrations of multiple analytes as they were spiked and diluted. This demonstration showed the feasibility of using LIBS for real-time liquid quantification models with estimated precision ≤ 8.1%. Finally, the limitations of this approach and potential future improvements are discussed.

Received 29th October 2024
Accepted 6th February 2025

DOI: 10.1039/d4ja00393d

rsc.li/jaas

1. Introduction

Chemical processing in the nuclear field (*e.g.*, reprocessing nuclear fuel or radioisotope separations), as well as many other fields, relies upon offline analytical measurements that can take days to weeks to complete. The implementation of optical spectroscopy, largely Raman spectroscopy and absorbance spectroscopy, for online process monitoring has grown due to its rapid measurement time and ability to be remotely deployed.[1] While these have been proven useful techniques, they can face challenges for species that lack viable absorption spectra, form varying oxidation states, or have weaker response functions. Plasma-based atomic emission methods offer potential alternatives for online measurements; this method is an alternative to solely relying on grab samples for traditional offline measurements. Such measurements are possible with solution cathode glow discharge[2–4] (SCGD) or laser-induced breakdown spectroscopy[5–7] (LIBS) approaches. LIBS can provide *in situ*, compositional measurements in milliseconds, providing operators with access to real-time information to more effectively control complex chemical systems. LIBS is performed by initially focusing a pulsed laser onto a sample surface or into a sample volume to form a microplasma. The optical emissions of this plasma are then collected and measured to provide an elemental signature of the sample. This measurement can be quantitative in nature with appropriate standards. LIBS is sensitive to most of the periodic table and can be applied to solids, liquids, gases, and aerosols.[5]

Unfortunately, liquids are the most challenging form of matter to investigate using LIBS.[8] This difficulty is due to the laser-induced plasma generating a shockwave, which disturbs the liquid surface, leading to shot-to-shot inconsistencies and potentially splashing liquid onto optical components. Researchers have overcome these challenges in various ways: using more complex optical configurations such as double

[a]*Radioisotope Science and Technology Division, Oak Ridge National Laboratory, Oak Ridge, Tennessee, USA. E-mail: andrewshb@ornl.gov*
[b]*Chemical Sciences Division, Oak Ridge National Laboratory, Oak Ridge, Tennessee, USA*
[c]*Biosciences Division, Oak Ridge National Laboratory, Oak Ridge, Tennessee, USA*

‡ Electronic supplementary information (ESI) available. See DOI: https://doi.org/10.1039/d4ja00393d

pulse (DP)-LIBS;[9–11] engineering the liquid sample to be in a repeatable form (*e.g.*, using a liquid jet);[9,12–15] using sheath gases to protect optical components from splashing;[16–18] drying liquid droplets (*i.e.*, surface-enhanced LIBS);[17,19–25] or forming an aerosol rather than measuring the liquid directly.[18,26–29] Although surface-enhanced LIBS and nanoparticle-enhanced LIBS have been demonstrated to substantially provide greater sensitivity by avoiding issues associated with liquid sampling, these methods are not amenable to real-time monitoring.[8] Furthermore, many engineered sampling methods have not been investigated for real-time monitoring. Thus, the goal of this study was to evaluate an engineered sampling system for real-time monitoring of process liquids and to investigate the approach to quantifying multiple elements in single samples and the sensitivity of this measurement approach.

This study introduces a novel approach for real-time, multielemental monitoring of liquid media using LIBS, incorporating a custom-engineered sampling system. First, a liquid wheel apparatus was employed to continuously refresh a thin liquid layer on a solid surface, ensuring consistent and reproducible LIBS measurements. The system was then modified to minimize liquid holdup in the transfer lines, addressing delays and inefficiencies associated with liquid transport. Second, these improvements were demonstrated through the univariate and multivariate calibration of the system for a variety of process monitoring relevant elements (Na, Al, K, Ca, Ti, Sr, Mo, and Yb). Finally, the direct online monitoring capabilities were demonstrated using mixed analyte solutions pumped through the liquid cell to quantify elemental composition. Overall, this study evaluates the use of an engineered sampling system to apply LIBS for real-time monitoring of liquid separations.

2. Experimental

2.1. Sample preparation

All samples were prepared from single-analyte 1000 μg mL^{-1} standards (High Purity Standards, Charleston, South Carolina) and subsequently diluted with deionized (DI) H_2O (18 MΩ cm^{-2}, NANOPure, Thermo Scientific). Experimental parameters were optimized using a multielement solution containing approximately 100 μg mL^{-1} of Na, Al, K, Ca, and Sr, as well as 1000 μg mL^{-1} Yb. For calibration, 40 mL of the most concentrated solution was pumped through the sample loop. Next, a serial dilution calibration was performed by iteratively removing 20 mL of the sample solution and then adding 20 mL of DI water to halve the concentration. An analytical sample (1 mL) was taken of each starting solution for verification measurements using inductively coupled plasma optical emission spectroscopy (ICP-OES, Thermo Scientific iCAP PRO, Bremen, Germany, see Table S1‡). The sample loop was rinsed with DI water three times when switching analytes to prevent cross contamination. Real-time validation tests were performed by continuously measuring the sample loop composition as it was spiked and diluted with various analytes. To begin, a 100 μg mL^{-1} Na solution was used. This solution was subsequently spiked with Ca, Sr, and K to reach nominal concentrations ranging from 40 to 80 μg mL^{-1} before diluting the solution by half with DI water. This test was used to investigate the online monitoring capabilities of LIBS in a simulated processing stream with transient conditions.

2.2. Liquid wheel LIBS configuration

A modified modular liquids sample chamber (SC-LQ2, Applied Photonics, UK) was used for liquid wheel-LIBS measurements. This method has been previously demonstrated but only in a single-analyte fashion and without the modifications made for real-time monitoring.[30] This system was equipped with a 100 mJ, 1064 nm Nd:YAG laser (Nano, Litron) and a broadband eight-channel spectrometer (Avantes, 4096CL). In this method, a liquid reservoir was filled with the sample solution, and a wedged wheel was continuously rotated through this liquid at rates ranging 1–10 rotations per minute (RPM), see Fig. 1. The wedged wheel was composed of stainless steel with a Ni plated exterior. The outer diameter of the wheel was approximately 50 mm and the angle of the wedge was approximately 40°. The rotational axis was connected to a linear translator for precise adjustment of the laser focal point relative to the wheel surface. Due to the angle of the wheel, a 1.0 mm lateral adjustment resulted in a 1.2 mm vertical adjustment of the wheel surface relative to the laser focal point.

Three gas nozzles were used to prevent droplet formation on the wheel, to spread the liquid across the wheel as a thin layer, and to prevent ablated liquid from accumulating on the optical window during testing. For this study, laboratory supplied compressed air was employed but future studies could explore the utilization of inert gases (*e.g.*, He). The laser was focused onto the wheel surface through an angled optical window to a spot size of approximately 500 μm. The plasma light was collected at a slight angle from the incident laser pulse. The sampling system parameters, including wheel rotation speed, gas flow rate, laser energy, spectrometer delay and integration times, and the number of shots, were optimized to maximize signal intensity. Spectra were measured at 10 Hz to maximize time resolution.

The liquid sample chamber was modified to reduce unused volume by changing the inlet and outlet lines to smaller tubing and using an alternative high-speed peristaltic pump (MP^2, Elemental Scientific Inc., Omaha, Nebraska) to add and remove solution from the sample cell. This change resulted in requiring approximately 40 mL to fill the sample cell for testing with minimal holdup in the liquid lines themselves. The peristaltic pump was connected to an external reservoir to provide a sampling loop, which would be amenable for online monitoring. The pump operated at a nominal flow rate of 10 mL min^{-1}. An illustration of the liquid wheel LIBS configuration is shown in Fig. 1.

2.3. Statistics and modeling

LIBS measurements are subject to the parameters used to form and measure the plasma emissions. These parameters are optimized by varying the settings and observing the spectral response. This spectral response is quantified using the signal-to-background ratio (SBR), in which the raw signal intensities are compared with the background intensities (eqn (1)):

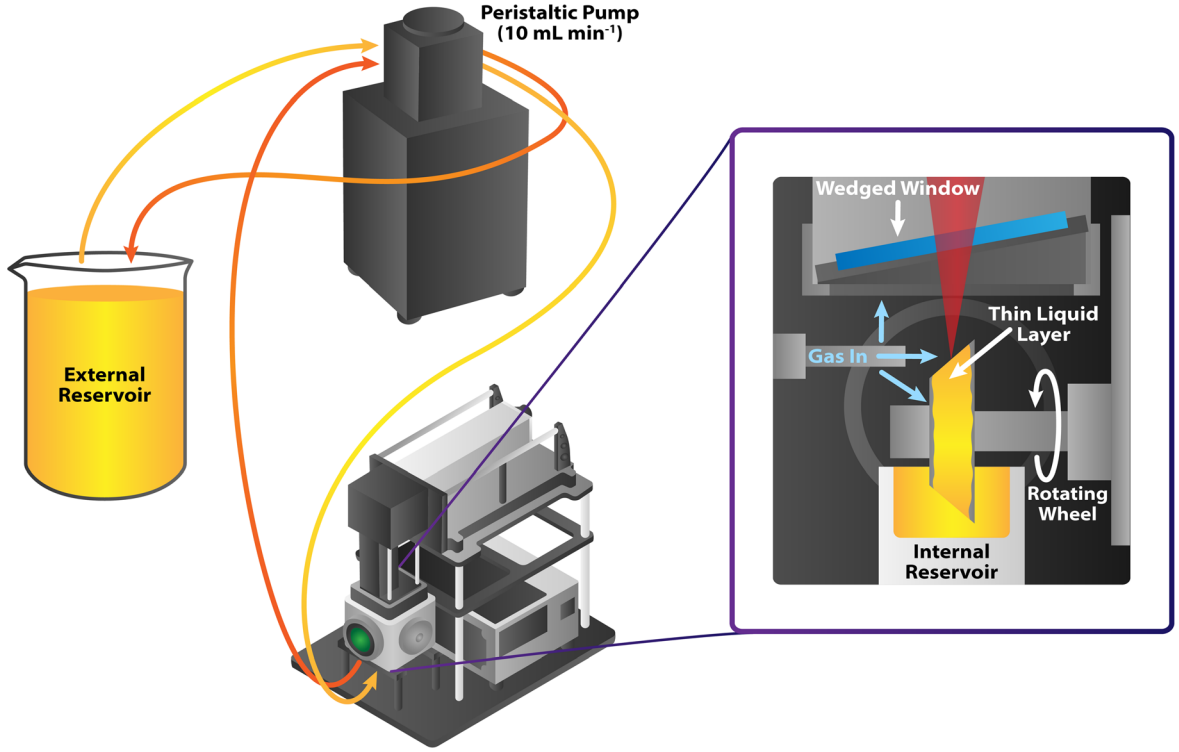

Fig. 1 Graphical representation of liquid LIBS sampling system showing the external and internal sample reservoirs connected using a peristaltic pump. The wedged wheel in the sample cell rotated through the internal reservoir, forming a thin liquid layer on the wheel for LIBS analysis. A gas nozzle was pointed at the surface of the wheel to help distribute the thin liquid layer at the ablation point to mitigate splashing and at the wedged window to prevent droplets from forming in the optical path.

$$\mathrm{SBR} = \frac{\text{signal intensity}}{\text{nearby baseline intensity}}. \quad (1)$$

For optimizing measurement parameters, both the SBR and its standard deviation (SD) were considered for all analytes (eqn (2)). For this analysis, the SBR and SD for each analyte were normalized to provide a score between zero and one. Then, the optimization score was taken as the summation of these normalized values weighted by 0.7 for SBR and 0.3 for SD. These weights were selected based on a desire for high signal strength and high precision; however, signal was given a slight preference because sensitivity was important.

$$\mathrm{SBR}_{\mathrm{norm}} = \frac{\mathrm{SBR}(i) - \mathrm{SBR}_{\mathrm{min}}}{\mathrm{SBR}_{\mathrm{max}} - \mathrm{SBR}_{\mathrm{min}}}, \quad (2a)$$

$$\mathrm{SD}_{\mathrm{norm}} = \frac{\mathrm{SD}_{\mathrm{max}} - \mathrm{SD}(i)}{\mathrm{SD}_{\mathrm{max}} - \mathrm{SD}_{\mathrm{min}}}, \quad (2b)$$

and

$$\mathrm{Score} = \sum_{\lambda_n}^{\lambda_N} 0.7 \times \mathrm{SBR}_{\mathrm{norm}} + 0.3 \times \mathrm{SD}_{\mathrm{norm}}. \quad (2c)$$

Calibration models were evaluated using various root mean square error (RMSE) metrics. RMSE serves as a measure of model prediction accuracy and is defined in eqn (3):

$$\mathrm{RMSE} = \sqrt{\frac{\sum (y_i - \hat{y}_i)^2}{n}}, \quad (3)$$

where y_i is the known sample concentration, $\hat{y}_i$ is the model predicted concentration, and n is the number of samples in the model. Several types of RMSE exist, all based on how they are calculated. The RMSE of calibration (RMSEC) measures how well a model fits training data; however, because all samples used to calculate RMSEC are included in the model, this method may overestimate prediction accuracy. RMSE of cross-validation (RMSECV) provides a more representative metric of model prediction accuracy by predicting samples not used in the training set. In this work, RMSECV was calculated by splitting the data into k groups, iteratively training the model on $k - 1$ groups, and then predicting the remaining k^{th} group. RMSE of prediction (RMSEP) takes the metric one step further by evaluating model accuracy on a separate validation dataset with samples never used for training.

Generally, LIBS has sensitivity to nearly every element in the periodic table, but the degree of sensitivity varies. The LODs of the models developed in this study were evaluated to benchmark this sampling approach. The univariate LODs were calculated using the standard error of the regression (S) and the calibration model coefficients (see eqn (4)). The use of the standard error of the regression has been shown to provide more accurate estimates of the LODs.[31]

$$\text{1st order } (y = m_1x + b),\ \text{LOD} = 3S, \tag{4a}$$

and

$$\text{2nd order } (y = m_1x^2 + m_2x + b),\ m_1\text{LOD}^2 + m_2\text{LOD} = 3S. \tag{4b}$$

Multivariate models were built using the SciKit Learn library in Python.[32] The number of latent variables (LVs) used in each model was determined using cross-validation (CV) and determining the last LV to provide a significant reduction in RMSECV. Model wavelength ranges were investigated along with the LVs through CV to optimize the model prediction metrics.

3. Results and discussion

3.1. Liquid wheel optimization

Prior to constructing calibration curves, the various parameters of the liquid wheel LIBS system required optimization. A sample containing 100 μg mL^{-1} of Na, Al, K, Ca, and Sr, as well as 1000 μg mL^{-1} Yb, was used for optimization. Parameters related to the sampling system itself included wheel rotation speed and sheath gas flow rate, which affected the formation of the thin liquid layer wheel. These parameters were optimized while keeping LIBS measurement parameters constant (100 mJ, 100 shot averages, 3 μs delay time, and 50 μs integration time). For optimization, both SBR and its SD for all the analytes were considered (see eqn (2)).

The optimization scores as a function of wheel rotation speed and sheath gas flow rate are shown in Fig. 2. The trends for individual analytes are shown in Fig. S1 and S2.‡ As an example of the effect of these parameters, the Sr 407.78 nm emission peak is shown as the wheel speed and gas flow rate are varied in Fig. 2. The optimal values were determined to be 2 RPM and 20 standard ft^3 h^{-1} (SCFH). A slower rotation speed provided far more intense spectra, likely because of more time for a consistent thin layer to form. Additionally, higher sheath gas flow rates provided the greatest optimization score, which may be attributed to enhanced thin layer formation or splashing reduction. Preliminary testing found that flow rates above 20 SCFH induced excessive evaporation in the chamber, causing solution concentrations to be affected. Note, for liquids with significantly different properties (*e.g.*, viscosity, wetting angle, *etc.*) these parameters would likely need to be reoptimized. Future work may investigate the use of this method on organic phases or inorganic phases with higher acid concentration where these effects would likely require separate or more complex models.

LIBS spectrometer parameters were then optimized using this rotation speed and gas flow rate. The laser energy was set to 100 mJ per pulse, and 100 shot accumulates were used, providing a spectrum every 10 s. Although the spectrometer settings could be optimized for each analyte individually, if several species were to be monitored simultaneously, an overall optimal value would be needed. The delay time was varied from

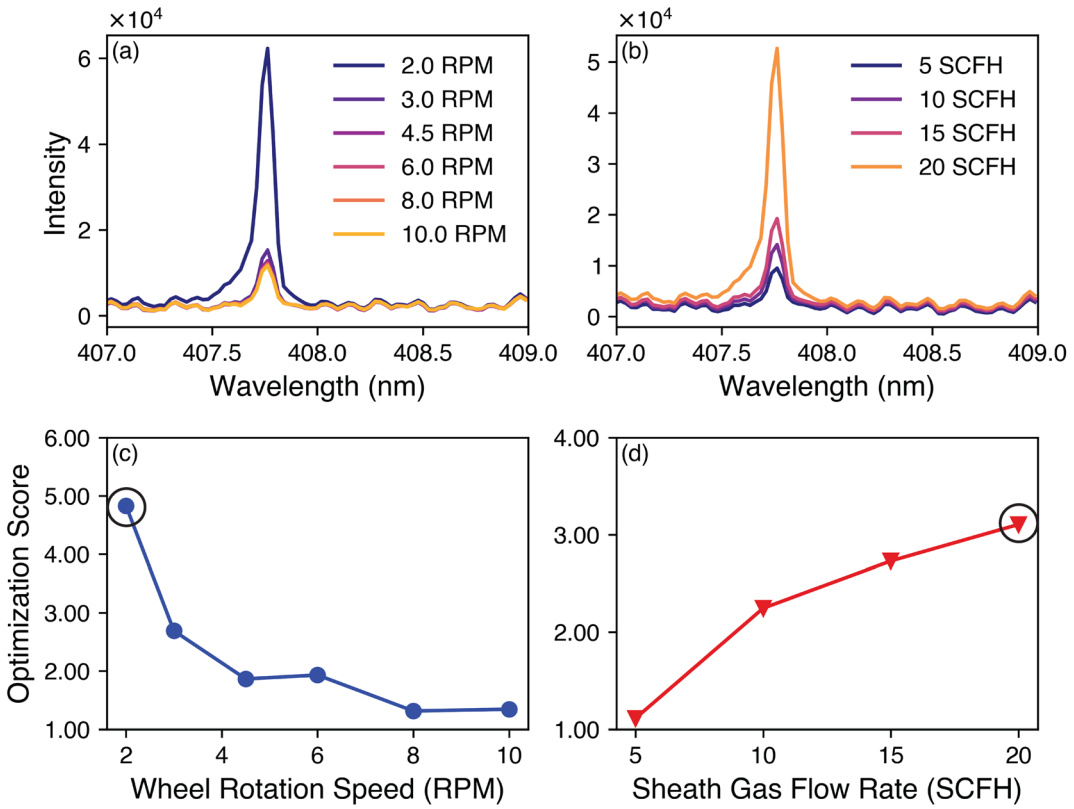

Fig. 2 Sr emission peaks and optimization scores as a function of (a and c) wheel rotation speed and (b and d) sheath gas flow rate. The optimization score used in this work considered both the SBR and SD of all analytes.

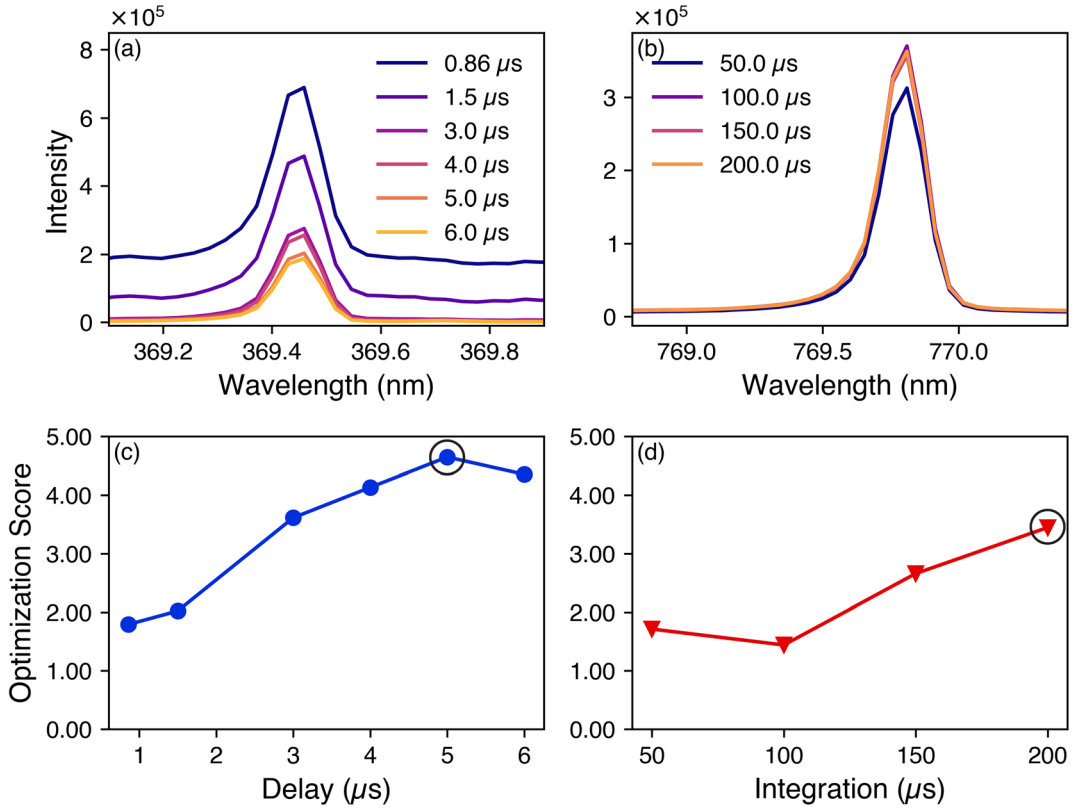

Fig. 3 (a) Yb and (b) K emission peaks as a function of delay time and integration times, respectively. The optimization scores for these variables are shown in (c) and (d). The selected settings are circled.

0.86 to 6 μs while keeping other settings constant (*e.g.*, 100 mJ, 100 shot average, and a 50 μs integration time). Similarly, the integration time was varied from 10 to 200 μs. The optimization scores for these settings are shown in Fig. 3, and trends for individual species are shown in Fig. S3.‡ The SBR increased as the delay time increased because of the decay of background light; SBR plateaued after 4 μs. The optimization score indicated that a 5 μs delay was optimal because of a decrease in deviation. The integration time had differing effects on various species, but several weaker-emitting species exhibited higher SBR values at extended integration times (Fig. S4‡). The optimization score indicated that a time of 200 μs should be used. The final optimal parameters to be used for the calibrations were identified as a 5 μs delay and a 200 μs integration time.

3.2. Liquid wheel calibration

Using these optimal settings, calibration curves for a series of selected species ranging from 1000 to 0 μg mL^{-1} were constructed through serial dilutions. The selected analytes were Na, Al, K, Ca, Ti, Sr, Mo, and Yb to include alkali metals, alkali earth metals, transition metals, a post-transition metal, and a lanthanide. The elements were carefully selected to represent important species across the periodic table but also with relevance to radioisotope chemical processing. For example, Na is typically uses as an additive to promote the separation of desired species into the organic phase; Al is a common impurity stemming from irradiated materials; and Yb is a lanthanide species used in the generation of the medical isotope ^{177}Lu. These species exhibited both weak and strong emission peaks across the spectrometer range, as well as a species also present in the wheel substrate (Mo). These calibration standards closely represent the inorganic phase of radiochemical separations and alternative models would need to be developed for organic phase monitoring.

The starting concentration was selected based on the peak intensity; analytes with stronger emission started at 400 μg mL^{-1}, and weaker peak calibrations began at 1000 μg mL^{-1}. This preference toward lower concentrations was targeted at identifying the detection limits of LIBS using this approach. At each concentration, 10 spectra were collected (each the average of 100 shots). Prior to modeling, spectra were baseline corrected using a rolling ball method with a 50-point radius to remove background light contributions.[33] The spectra were then smoothed using a Savitzky–Golay filter with a five-point window and a third-order polynomial.

For each element, univariate models were built using each species' strongest emission peak. Note, integrated peak area was used rather than peak intensity for univariate calibration to make models more robust. These peaks were Na I at 588.9 nm, Al I at 396.2 nm, K I at 766.5 nm, Ca I at 393.5 nm, Ti II at 334.9 nm, Sr II at 407.8 nm, Mo I at 550.6 nm, and Yb II at 369.4 nm. Generally, peaks without interferences were used, but in the case of Mo, unavoidable interferences occurred because

of the wheel material. All emission wavelengths were confirmed against the National Institute of Standards and Technology Atomic Spectral DataBase.[34] These emission peaks as a function of the calibration concentration are shown in Fig. 4, along with an exemplary full spectrum. Notably, this liquid wheel sampling method does involve ablation of the wheel material itself. If the targeted analyte has overlapping emissions with the alloy components, then an alternate wheel or a coating on the wheel may need to be identified. To better understand these effects, both an element (Mo) in the wheel and an element (Ti) with interferences from the wheel were investigated.

Several peaks (*e.g.*, Na, Ca, K) exhibited nonlinear calibrations because of self-absorption effects. These analytes were modeled using a second-order polynomial only if a first-order model could not provide an adequate fit. If a second-order polynomial was used, the calibration range was truncated after fitting to exclude the most concentrated sample to avoid overfitting issues. The univariate calibration models along with their R^2 values are shown in Fig. 5.

The univariate calibration metrics are provided in Table 1. The RMSECV values were calculated using a leave-one-out-CV approach. Elements that exhibited strong emission peaks (*i.e.*, Na, Ca, and K) generated excellent univariate fits with strong R^2 values and low RMSEC scores. Because RMSE values vary in magnitude based on the calibration range of the analyte, they can be more readily compared by dividing the values by the concentration range of the respective calibration and viewed as a percent (RMSE%). In this work, a model can be ranked based

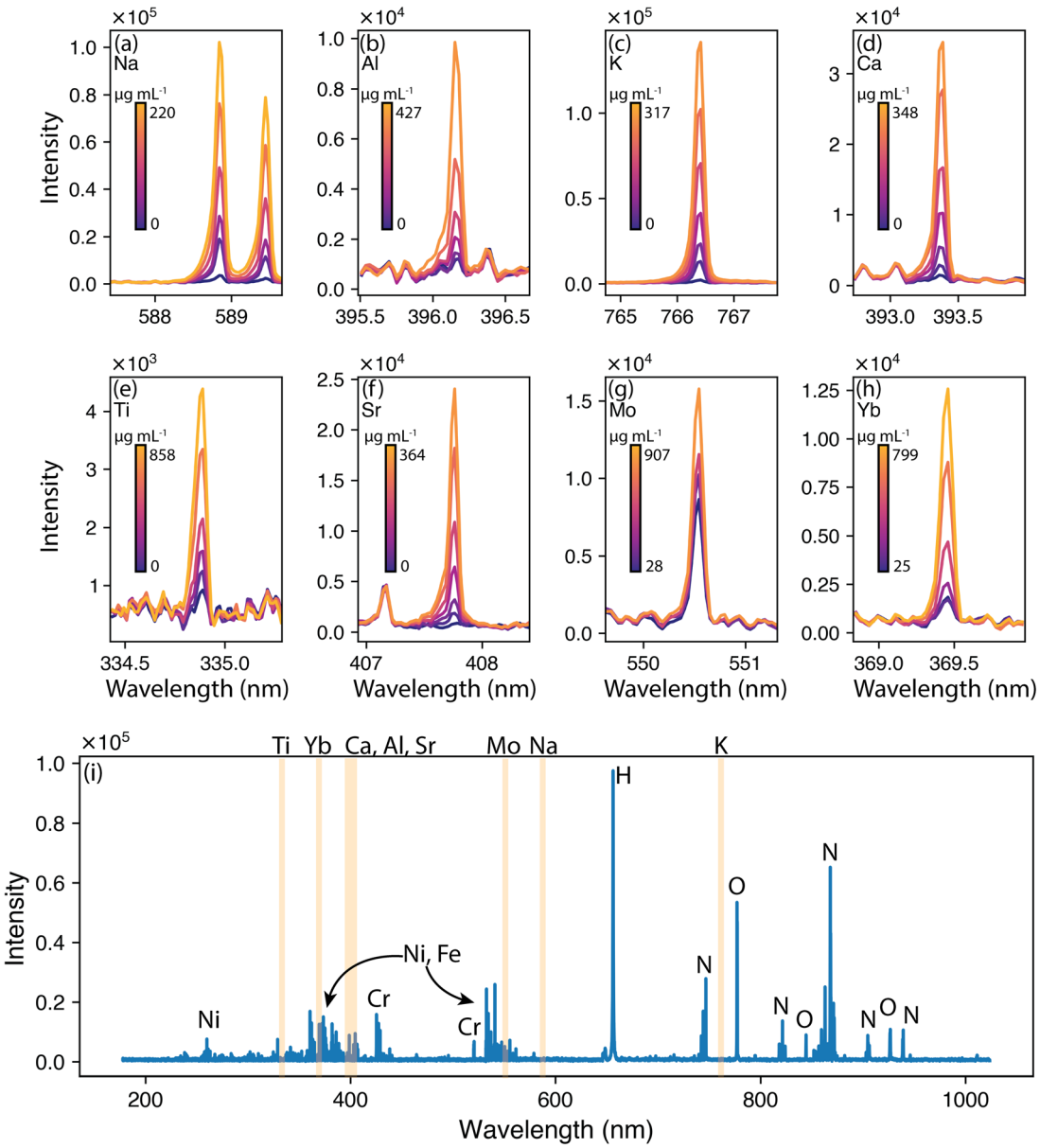

Fig. 4 Emission peaks as a function of concentration: (a) Na, (b) Al, (c) K, (d) Ca, (e) Ti, (f) Sr, (g) Mo, and (h) Yb. The full labeled spectrum of a DI H_2O sample (blank) is shown in (i) with analyte regions of interest highlighted.

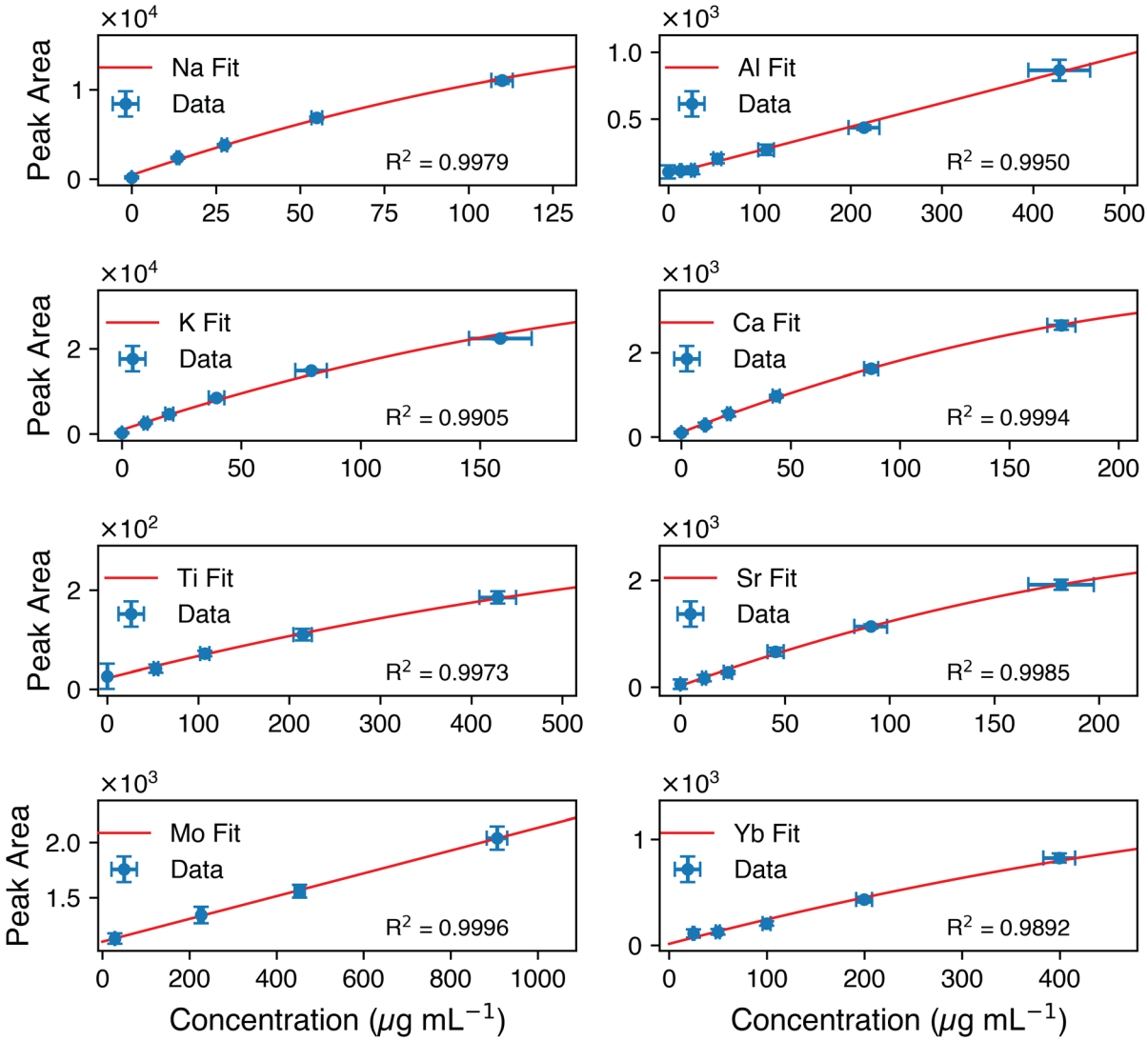

Fig. 5 Univariate calibration curves for (top left to bottom right) Na, Al, K, Ca, Ti, Sr, Mo, and Yb. The R^2 values of each calibration model are provided. *X* error is propagated uncertainty from ICP-OES measurements, and *Y* error is the peak area uncertainty.

Table 1 Univariate model metrics[a]

Analyte	R^2	RMSEC (μg mL^{-1})	RMSECV (μg mL^{-1})	LOD (μg mL^{-1})	RMSEC (%)	RMSECV (%)
Na^2	0.9979	1.76	4.00	0.0532	1.76	4.00
Al^1	0.9950	10.2	57.9	18.5	2.54	14.5
K^2	0.9905	5.29	11.6	0.105	2.65	5.78
Ca^2	0.9994	1.51	2.35	0.273	0.75	1.18
Ti^2	0.9973	7.91	15.1	67.7	1.58	3.03
Sr^2	0.9985	2.44	3.23	0.640	1.22	1.62
Mo^1	0.9996	6.65	159	22.4	0.67	15.9
Yb^2	0.9892	14.2	32.3	22.9	1.77	4.04

[a] The superscripted numbers on the analyte labels refer to the univariate model rank (*e.g.*, 2 = second order). For model concentration ranges the reader is referred to Fig. 5.

on RMSE%: strong (RMSE% ≤ 5%), satisfactory (5 < RMSE% ≤ 10%), or indicative (10% < RMSE% ≤ 15%). Based on the RMSEC% values shown in Table 1, all models would be ranked as strong; however, percent RMSECV (RMSECV%) is a better metric for predicting unknown samples. In this study, the models for Na, Ca, Sr, Yb, and Ti would be ranked as strong; K

would be ranked as satisfactory; and Al would be ranked as indicative. The model for Mo falls beyond the indicative range based on RMSECV%, which can be attributed to the effects of the wheel interferences. Notably, Al and Mo were modeled using a first-order linear fit, meaning the highest concentration had an increased leverage. This indicates that adding more model points would likely enhance the predictive capabilities.

To better evaluate the LODs of this engineered sampling approach, the univariate LODs were compared with literature values shown in Table 2. Literature values were only used for comparison if they were measured on bulk liquids or an alternative engineered approach. Surface-enhanced LIBS and similar approaches (*e.g.*, dried droplets, frozen droplets, nanoparticle enhanced LIBS) were not considered.

Overall, half of the species investigated resulted in lower than microgram per milliliter LODs, and the remainder except for Ti fell below 50 μg mL^{-1}. In terms of process monitoring, these LODs offer much value. Several elements (*e.g.*, Na, Al, and Ca) have been studied extensively in liquid LIBS; for these analytes, the liquid wheel sampling approach appeared to provide detection limits on par with literature values. For lesser-studied elements (*e.g.*, Sr and Yb), the liquid wheel approach offered lower LODs than literature. Although the LOD for K is higher than the literature-reported value, it is less than the

Table 2 Summary of LODs compared with literature values[a]

Element	Literature liquid LIBS LOD (μg mL^{-1})	This study (μg mL^{-1})
Na	0.0075–24 (ref. 38–43)	0.0532
Al	15–35 (ref. 39, 42 and 44)	18.5
K	0.0012 (ref. 44)	0.105
Ca	0.002–10 (ref. 40–42 and 45)	0.273
Ti	9.3–18.8 (ref. 42)	67.7
Sr	25–200 (ref. 46)	0.640
Mo	31 (ref. 42)	22.4
Yb	156 (ref. 47)	22.9

[a] LODs from surface-enhanced LIBS approaches were not included.

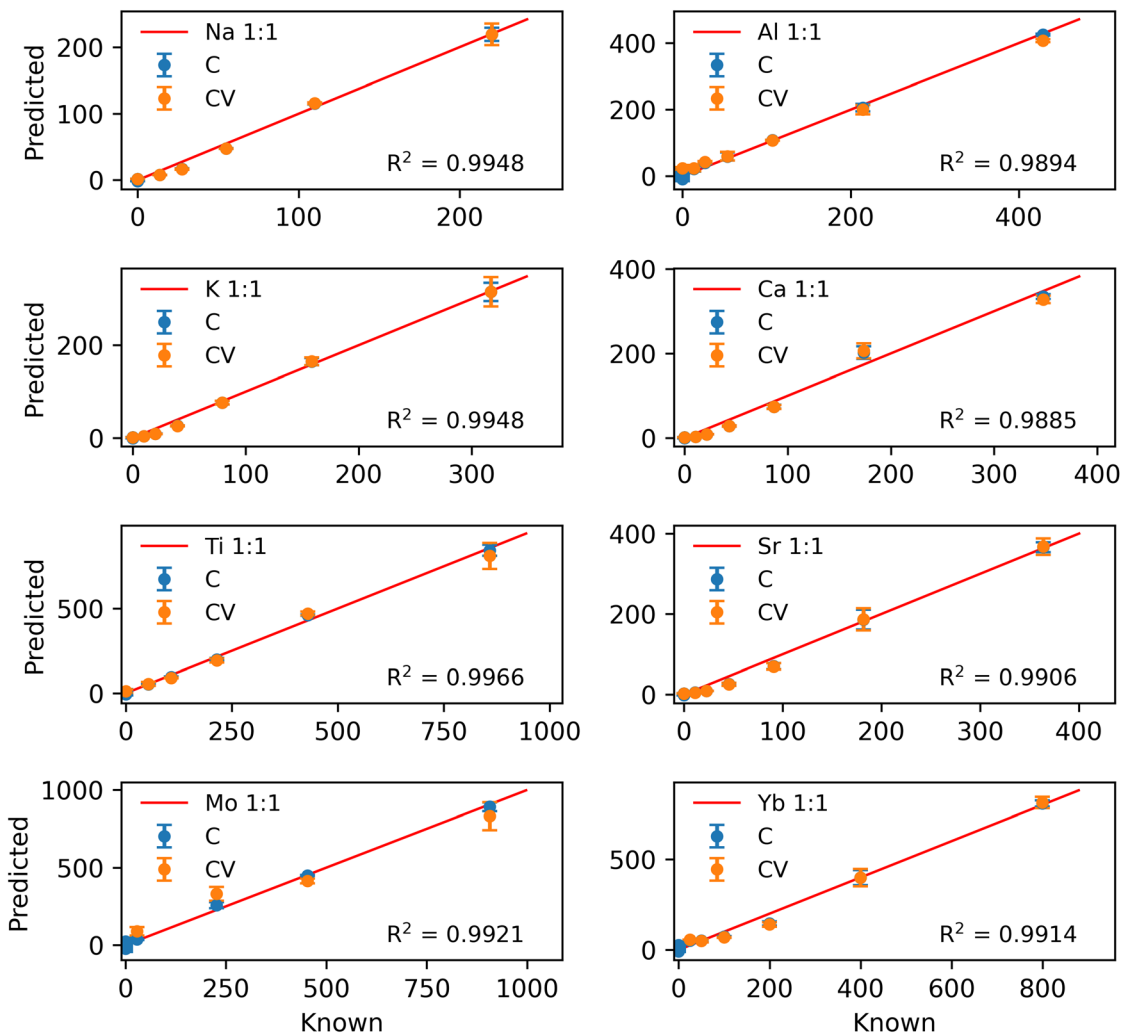

Fig. 6 PLSR parity plots comparing known values with predicted concentrations (μg mL^{-1}) for (top left to bottom right) Na, Al, K, Ca, Ti, Sr, Mo, and Yb. The red 1 : 1 line denotes a perfect prediction. The R^2 values of each calibration model are provided. C markers refer to calibration data points, and CV markers refer to cross-validation data points.

microgram per milliliter level, demonstrating an LOD comparable with other high-performance techniques. Despite generating a strong fit, the Ti model provided LODs above literature values. Ti offered weaker emissions and was in a spectral region with a large density of emission peaks from the wheel material, which likely led to this higher detection limit. Lastly, the LODs reported here are on par with the levels expected (*i.e.*, low- to sub-μg mL^{-1}) for typical instances of other optical spectroscopic methods for online monitoring (*e.g.*, Raman, UV-VIS, NIR, LIFS).[35–37] Several of the species investigated have difficulties being measured using other methods. For example, Yb lacks a usable absorbance profile in the visible range. Realistically, LIBS would be combined with multiple other techniques in targeted process locations to provide a holistic picture of the process compositions based on the operator's needs.

To build more robust models, multivariate models were also investigated. Multivariate models are typically useful for LIBS data that have a high dimensionality (*i.e.*, wavelength dimension) *versus* the response dimension (concentration).[48] Furthermore, multivariate models can incorporate the signal from multiple emission peaks and better account for interferences. Partial least squares regression (PLSR) is a well-established chemometric model for multivariate modeling.[49,50] PLSR iteratively solves for vectors (*i.e.*, LVs), which explain the most covariance between the signal and response matrix (*i.e.*, concentration), making the method well-suited for predictive models.

Based on the anticipated second-order effects caused by self-absorption, the spectral matrix was augmented to include second-order features by appending the squared spectra to the regressed data block. To ensure proper modeling, both the spectra and squared spectra data blocks were scaled using a hard-block variance approach before being combined.[51] Future work could investigate kernel partial least squares (PLS) as an alternative approach for nonlinear PLS models.[52] The calibration and CV parity plots for each element's PLSR model, along with R^2 values, are shown in Fig. 6. Further details on the PLSR models are provided in the Table S2.‡ The multivariate model metrics are provided in Table 3.

Where the univariate models were only built using the calibration samples for a given analyte, each PLSR model was built with the entire dataset, containing all analytes, to be more robust to additional species. All models generated excellent fits with R^2 values greater than 0.98. When the RMSECV% values were considered, all models except for Mo fell into the strong ranking. This result reaffirmed that the multivariate models can better cope with interferences and weak signals (*e.g.*, Ti and Al) compared with univariate models. However, even with this improvement, the Mo model is still only considered satisfactory. Another benefit is that modeling the second-order behavior in this multivariate manner did not truncate the calibration range as in the univariate case, although model performance at the edges of the design space were weaker during CV (see Fig. 5 [Ti]).

Table 3 Multivariate model metrics[a]

Analyte	R^2	RMSEC (μg mL^{-1})	RMSECV (μg mL^{-1})	RMSEC (%)	RMSECV (%)
Na^2	0.9948	2.51	7.31	1.25	3.65
Al^1	0.9894	6.98	13.4	1.74	3.36
K^2	0.9948	3.61	9.21	0.90	2.30
Ca^2	0.9885	5.90	14.7	1.48	3.67
Ti^2	0.9966	7.92	25.8	0.79	2.58
Sr^2	0.9906	5.59	14.0	1.40	3.49
Mo^1	0.9921	12.8	69.9	1.28	6.99
Yb^2	0.9914	11.7	30.6	1.17	3.06

[a] The superscripted numbers on the analyte labels refer to the spectral transformation rank (*e.g.*, 2 = second order). For model concentration ranges the reader is referred to Fig. 6.

3.3. Real-time validation tests

As a final evaluation of this liquid LIBS approach being amenable to online monitoring, a real-time validation test was performed in which the sample reservoir outside of the LIBS system was spiked and diluted to generate transient signals with multiple analytes as the solution was pumped into the LIBS chamber. The test began with a 100 μg mL^{-1} Na solution, and then the reservoir was sequentially spiked with Ca, Sr, and K. The last step was diluting the sample reservoir by doubling the volume of water.

The test provided significant insight into the real-time monitoring capabilities of the sampling approach. Notably, the contribution of the wheel emissions to the overall spectra was more than in the previous calibration datasets, likely because of the extended use of this ablation substrate (>200 000 shots). This higher contribution resulted in the previous PLSR models underpredicting the sample concentrations. The models were recalibrated using a total light normalization scheme in which each spectrum was divided by the sum of all intensities in said spectrum, similar to L_1 normalization. This process, along with slight modifications to the number of LVs for the models to be more robust to the substrate signal, provided accurate predictions. These PLSR predictions *versus* expected concentration profiles are shown in Fig. 7. Information on the modified PLSR models is provided in Table S3.‡

The starting sample reservoir volume was 40 mL. Based on the transient predictions, the concentration changes were resolved in roughly 4 min, corresponding to the amount of time for the sample volume to fully circulate at 10 mL min^{-1}. The final step corresponding to the dilutions of each analyte showed an extended rate of change because of the increase in sample volume. Lastly, the model precision can be evaluated by examining the percent relative standard deviation (% RSD) of the predictions during the time between the third and fourth additions (t = 45–65 min in Fig. 7, 120 points total), during which analyte concentrations had stabilized: Na = 3.1%, K = 4.2%, Ca = 8.1%, and Sr = 7.4%. These results demonstrate that LIBS can provide reliable predictions despite spectral fluctuations owing to factors such as laser power variance.

Despite these positive outcomes, areas for improvement must be acknowledged. The constant ablation of the wheel substrate leads to a consumable component in the sampling

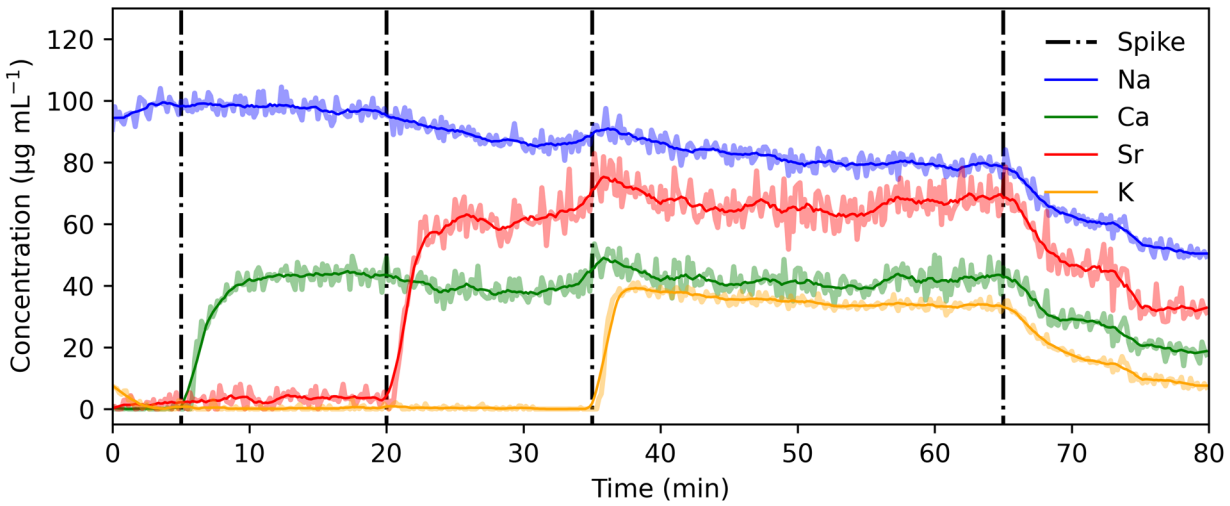

Fig. 7 PLSR predictions during the real-time test. The transparent lines represent the PLSR predictions as the data were collected (*i.e.*, 100 shot average per second), and the darker lines represent the running average. The solid black dashed lines indicate when the sample reservoir was spiked.

system. For specific applications, robust models can be made to cope with these changes with minimal detriment, but for other fields (*e.g.*, radiological hot cells), the replacement of this component could serve as a barrier for adoption. The use of an internal standard may aid in coping with these effects but is again only applicable in certain situations. Finally, the sample cell was operable with volumes as low as 20 mL, but for the measurement of precious samples (*e.g.*, rare isotope processing streams), this amount can still be too high a volume for adoption. However, this volume may be reduced further with additional modifications.

4. Conclusion

LIBS is commonly boasted as a versatile elemental technique with a large breadth of sensitivity and the ability to be applied to all forms of matter; however, the bulk of LIBS literature revolves around solid-phase analysis, where the technique excels. This study examined an engineered sampling approach in which a rotating wheel provides a constantly refreshing thin liquid layer for measurements. Both univariate and multivariate models for eight elements from across the periodic table (Na, Al, K, Ca, Ti, Sr, Mo, and Yb) were constructed. This setup allowed the LOD for each analyte to be investigated, revealing that this sampling approach can offer LODs ranging from the hundreds of parts per billion to the low parts per million levels. This range falls in line with other literature-reported LOD values on bulk liquids and other engineered sampling schemes. Lastly, this approach for online monitoring of impurities in chemical processing systems was examined through an 80 min real-time test demonstrating reliable predictions with prediction precision below 10% RSD.

Future work should examine these analytes using alternative sampling systems that do not rely on ablation substrates. For example, the conversion of liquids to aerosols or liquid jets are viable for online monitoring approaches using LIBS. Additionally, literature has demonstrated increased sensitivity with DP-LIBS. It may be feasible to reach lower LODs with less ablation of the rotating wheel using DP-LIBS. Finally, alternate wheel materials and passive coatings thereof should be investigated to extend the component lifetime and reduce interferences.

Data availability

All relevant data that support these experimental findings are available from the corresponding author upon reasonable request.

Author contributions

Conceptualization (H. A., L. S.), data curation (H. A., Z. K.), formal analysis (H. A.), funding acquisition (H. A., L. S., M. M.), investigation (H. A., Z. K., L. S., B. M.), methodology (H. A., Z. K.), visualization (H. A.), writing – original draft (H. A., Z. K.), writing – review & editing (H. A., Z. K., L. S., B. M., M. M.)

Conflicts of interest

The authors declare no competing interests.

Acknowledgements

The authors would like to acknowledge Jacquelyn Demink for assistance with graphics. This research was supported by the US Department of Energy Isotope Program, managed by the Office of Science for Isotope R&D and Production.

References

1 P. Tse, N. P. Bessen, G. B. Hall, B. N. Seiner, G. J. Lumetta, S. A. Bryan and A. M. Lines, *Solvent Extr. Ion Exch.*, 2024, **42**, 347–380.
2 M. R. Webb, F. J. Andrade and G. M. Hieftje, *Anal. Chem.*, 2007, **79**, 7807–7812.

3 M. R. Webb, F. J. Andrade and G. M. Hieftje, *Anal. Chem.*, 2007, **79**, 7899–7905.
4 B. Wiggershaus, M. Jeskanen, A. Roos, T. Laurila and C. Vogt, *J. Anal. At. Spectrom.*, 2025, **40**, 338–345.
5 D. W. Hahn and N. Omenetto, *Appl. Spectrosc.*, 2012, **66**, 347–419.
6 D. W. Hahn and N. Omenetto, *Appl. Spectrosc.*, 2010, **64**, 335A–366A.
7 E. H. Kwapis, J. Borrero, K. S. Latty, H. B. Andrews, S. S. Phongikaroon and K. C. Hartig, *Appl. Spectrosc.*, 2024, **78**, 9–55.
8 K. Keerthi, S. D. George, S. D. Kulkarni, S. Chidangil and V. Unnikrishnan, *Opt Laser. Technol.*, 2022, **147**, 107622.
9 A. Kumar, F. Y. Yueh and J. P. Singh, *Appl. Opt.*, 2003, **42**, 6047–6051.
10 V. N. Rai, F.-Y. Yueh and J. P. Singh, *Appl. Opt.*, 2003, **42**, 2094–2101.
11 M. Siemens, B. Emde, M. Henkel, R. Methling, S. Franke, D. Gonzalez and J. Hermsdorf, *Physics*, 2024, **6**, 108–122.
12 K. Skočovská, J. Novotný, D. Prochazka, P. Pořízka, K. Novotný and J. Kaiser, *Rev. Sci. Instrum.*, 2016, **87**, 043116.
13 Y. Feng, J. Yang, J. Fan, G. Yao, X. Ji, X. Zhang, X. Zheng and Z. Cui, *Appl. Opt.*, 2010, **49**, C70–C74.
14 R. Nakanishi, H. Ohba, M. Saeki, I. Wakaida, R. Tanabe-Yamagishi and Y. Ito, *Opt. Express*, 2021, **29**, 5205–5212.
15 C. R. Bhatt, D. Hartzler, J. Jain and D. L. McIntyre, *Appl. Phys. B:Lasers Opt.*, 2021, **127**, 8.
16 P. Fichet, M. Tabarant, B. Salle and C. Gautier, *Anal. Bioanal. Chem.*, 2006, **385**, 338–344.
17 H. A. Harun and R. Zainal, *J. Nonlinear Opt. Phys. Mater.*, 2018, **27**, 1850023.
18 H. B. Andrews and K. G. Myhre, *Appl. Spectrosc.*, 2022, **76**, 877–886.
19 K. Liu, Z. Tang, R. Zhou, W. Zhang, Q. Li, C. Zhu, C. He, K. Liu and X. Li, *J. Anal. At. Spectrom.*, 2021, **36**, 2480–2484.
20 D. J. Palásti, P. Albrycht, P. Janovszky, K. Paszkowska, Z. Geretovszky and G. Galbács, *Spectrochim. Acta, Part B*, 2020, **166**, 105793.
21 Y. Chen, J. Si, X. Wan, Y. Wang, A. Chen and M. Jin, *Spectrochim. Acta, Part B*, 2024, **213**, 106880.
22 S. Irvine, H. Andrews, K. Myhre and J. Coble, *J. Quant. Spectrosc. Radiat. Transfer*, 2023, **297**, 108486.
23 H. B. Andrews, L. R. Sadergaski and K. G. Myhre, *J. Anal. At. Spectrom.*, 2022, **37**, 768–774.
24 D. Alamelu, A. Sarkar and S. Aggarwal, *Talanta*, 2008, **77**, 256–261.
25 A. Sarkar, D. Alamelu and S. K. Aggarwal, *Appl. Opt.*, 2008, **47**, G58–G64.
26 H. B. Andrews, J. McFarlane and K. G. Myhre, *Appl. Spectrosc.*, 2022, **76**, 988–997.
27 E. M. Cahoon and J. R. Almirall, *Anal. Chem.*, 2012, **84**, 2239–2244.
28 X. Yang, X. Wang, D. Li, X. Zhang, K. Li, H. Ren, Z. Zhou, Z. Qin and X. Zheng, *J. Anal. At. Spectrom.*, 2024, **39**, 433–438.
29 H. Ji, Y. Ding, L. Zhang, Y. Hu and X. Zhong, *Appl. Spectrosc. Rev.*, 2021, **56**, 193–220.
30 X. Cama-Moncunill, M. Markiewicz-Keszycka, P. J. Cullen, C. Sullivan and M. P. Casado-Gavalda, *Food Chem.*, 2020, **309**, 125754.
31 D. B. Hibbert and J. J. Gooding, *Data Analysis for Chemistry: an Introductory Guide for Students and Laboratory Scientists*, OUP, USA, 2006.
32 F. Pedregosa, G. Varoquaux, A. Gramfort, V. Michel, B. Thirion, O. Grisel, M. Blondel, P. Prettenhofer, R. Weiss and V. Dubourg, *J. Mach. Learn. Res.*, 2011, **12**, 2825–2830.
33 K. H. Liland, T. Almøy and B.-H. Mevik, *Appl. Spectrosc.*, 2010, **64**, 1007–1016.
34 Y. Ralchenko, A. Kramida, J. Reader and NIST ASD Team, *NIST Atomic Spectra Database, Version 5.12*, National Institute of Standards and Technology, Gaithersburg, MD2024, DOI: **10.18434/T4W30F**, available: **https://physics.nist.gov/asd**.
35 A. M. Lines, H. M. Felmy, S. A. Bryan and M. J. Minette, *Raman Spectroscopy Based On-Line, Real-Time Monitoring to Reduce Composition Uncertainties: Enhanced Sensitivity through Optimization of Raman Parameters*, Pacific Northwest National Laboratory (PNNL), Richland, WA (United States), 2021.
36 H. B. Andrews and L. R. Sadergaski, *ACS Sens.*, 2024, **9**, 6257–6264.
37 L. R. Sadergaski and H. B. Andrews, *Analyst*, 2022, **147**, 4014–4025.
38 D. Zhu, L. Wu, B. Wang, J. Chen, J. Lu and X. Ni, *Appl. Opt.*, 2011, **50**, 5695–5699.
39 R. Knopp, F. Scherbaum and J. Kim, *Fresenius' J. Anal. Chem.*, 1996, **355**, 16–20.
40 O. Samek, D. C. Beddows, J. Kaiser, S. V. Kukhlevsky, M. Liska, H. H. Telle and A. J. Whitehouse, *Opt. Eng.*, 2000, **39**, 2248–2262.
41 A. De Giacomo, M. Dell'Aglio and O. De Pascale, *Appl. Phys. A:Mater. Sci. Process.*, 2004, **79**, 1035–1038.
42 P. Yaroshchyk, R. J. Morrison, D. Body and B. L. Chadwick, *Spectrochim. Acta, Part B*, 2005, **60**, 986–992.
43 D. Zhang, Z. Hu, Y. Su, B. Hai, X. Zhu, J. Zhu and X. Ma, *Opt. Express*, 2018, **26**, 18794–18802.
44 D. A. Cremers, L. J. Radziemski and T. R. Loree, *Appl. Spectrosc.*, 1984, **38**, 721–729.
45 B. Charfi and M. Harith, *Spectrochim. Acta, Part B*, 2002, **57**, 1141–1153.
46 A. M. Popov, A. N. Drozdova, S. M. Zaytsev, D. I. Biryukova, N. B. Zorov and T. A. Labutin, *J. Anal. At. Spectrom.*, 2016, **31**, 1123–1130.
47 C. R. Bhatt, J. C. Jain, C. L. Goueguel, D. L. McIntyre and J. P. Singh, *Spectrochim. Acta, Part B*, 2017, **137**, 8–12.
48 V. Palleschi, *Chemometrics and Numerical Methods in LIBS*, Wiley Online Library, 2023.
49 I. S. Helland, *Scand. J. Stat.*, 1990, 97–114.
50 P. Geladi and B. R. Kowalski, *Anal. Chim. Acta*, 1986, **185**, 1–17.
51 M. P. Campos and M. S. Reis, *Chemom. Intell. Lab. Syst.*, 2020, **199**, 103959.
52 R. Rosipal, *Chemoinformatics and Advanced Machine Learning Perspectives: Complex Computational Methods and Collaborative Techniques*, 2011, pp. 169–189.